Akuhara *et al. Earth, Planets and Space* (2021) 73:171
https://doi.org/10.1186/s40623-021-01501-5

Earth, Planets and Space

FULL PAPER

Open Access

Lithosphere–asthenosphere boundary beneath the Sea of Japan from transdimensional inversion of S-receiver functions

Takeshi Akuhara[1*], Kazuo Nakahigashi[2], Masanao Shinohara[1], Tomoaki Yamada[1], Hajime Shiobara[1], Yusuke Yamashita[3], Kimihiro Mochizuki[1] and Kenji Uehira[4]

Abstract

The evolution history of the Sea of Japan back-arc basin remains under debate, involving the opening of sub-basins such as the Japan and Yamato Basins. Detailed knowledge of the lithospheric structure will provide the key to understanding tectonic history. This study identifies the lithosphere–asthenosphere boundary (LAB) beneath the Sea of Japan back-arc basin using S-receiver functions (S-RFs). The study area, including the Japan and Yamato Basins, has been instrumented with broadband ocean-bottom seismometers (OBSs). S-RFs from these OBSs show negative Sp phases preceding the direct S arrivals, suggesting the LAB. The S-RFs also show abnormally reduced amplitudes. For further qualitative interpretation of these findings, we conduct transdimensional Bayesian inversion for S-wave velocity models. This less-subjective Bayesian approach clarifies that the low-velocity seafloor sediments and damped deconvolution contribute to the amplitude reduction, illuminating the necessity of such considerations for similar receiver function works. Inverted velocity structures show a sharp velocity decrease at the mantle depths, which we consider the LAB. The obtained LAB depths vary among sites: ~ 45 km beneath the Japan and Yamato Basins and ~ 70 km beneath the Yamato Rise, a bathymetric high between the two basins. The thick lithosphere beneath the Yamato Rise most likely reflects its continental origin. However, the thickness is still thin compared to that of eastern Asia, suggesting lithosphere extension by rifting. Notably, the Japan and Yamato Basins show a comparable lithospheric thickness, although the crustal thickness beneath the Yamato Basin is known to be anomalously thick. This consistency in the lithospheric thickness implies that both basins undergo similar back-arc opening processes.

Keywords: Back-arc basin, Lithosphere–asthenosphere boundary, Sea of Japan, S-receiver function, Transdimensional inversion, Ocean-bottom seismometer

Background

The Sea of Japan, located between the Japanese island arc and Asia's eastern margin, hosts three sub-basins (Japan, Yamato, and Tsushima Basins) and a topographic high (the Yamato Rise) (Fig. 1). The sea evolved through rifting and back-arc spreading, which have isolated Japanese Islands from Asia's continent. The rifting is likely to have begun at ~ 23 Ma, and the whole opening process ceases at ~ 15 Ma (Martin 2011; Van Horne et al. 2017), where clues come from various disciplines including radiometric dating for core samples (Tamaki et al. 1990), paleomagnetism from rocks (Otofuji et al. 1985) and the seafloor (Seama and Isezaki 1990), dike, vein, and fault orientations (Sato 1994), and migration of a volcanic front (Tatsumi et al. 1989). However, limited

*Correspondence: akuhara@eri.u-tokyo.ac.jp
[1] Earthquake Research Institute, The University of Tokyo, 1-1-1, Yayoi, Bunkyo-ku, Tokyo 113-0032, Japan
Full list of author information is available at the end of the article

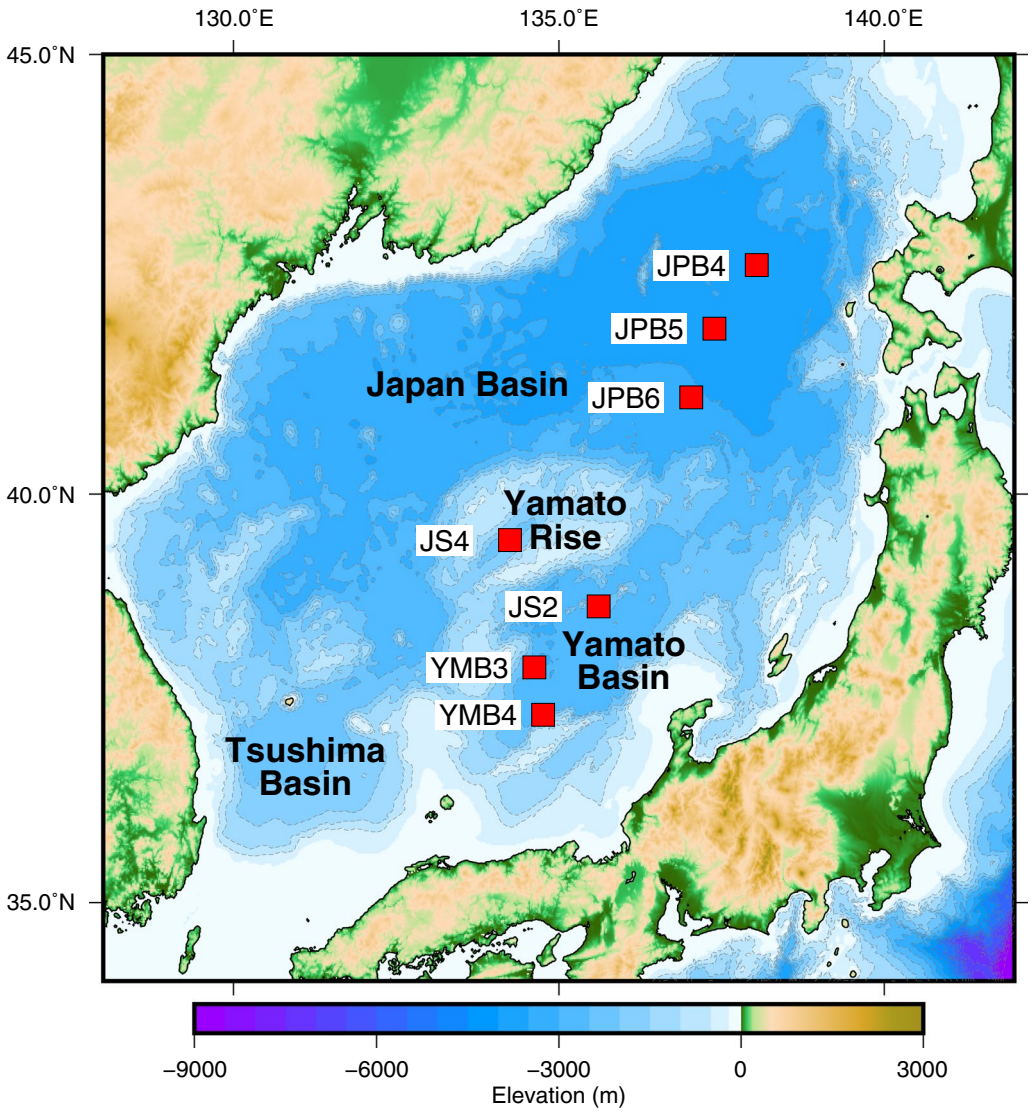

Fig. 1 Tectonic setting of the study area and station arrangement. Red squares denote observation sites where broadband seismometers were deployed

spatiotemporal resolution of these data makes the comprehensive understanding of the evolution process challenging. A major consensus is that back-arc spreading contributes to the formation of the Japan Basin, as is implied from the lineation pattern in the seafloor magnetic anomaly. In contrast, the formation processes of the Yamato and Tsushima basins are still open questions because of unclear magnetic anomaly and anomalous features of the crust, as introduced below.

Many active-source seismic surveys have revealed crustal structure at the Sea of Japan (Hirata et al. 1989; Kurashimo et al. 1996; Sato et al. 2006, 2018; Nakahigashi et al. 2013) and also have provided unique constraints on the evolution process. At the Japan Basin, the crust has a typical thickness of ~ 7 km for the oceanic crust, whereas the crust at the Yamato and Tsushima Basins is anomalously thick with a thickness of ~ 15 km. Although the origin of these anomalous crusts is still puzzling, their relatively high P-wave velocities (Vp) resemble typical oceanic crusts than continental crusts (Sato et al. 2018). Hirata et al. (1989) has attributed the cause of this thickened crust to an excess magma supply after the termination of the seafloor spreading, which follows the abrupt tectonic reversal to the compressional field at ~ 15 Ma (Sato 1994). The Yamato Rise is a region with the thickest crusts in the sea with a thickness of ~ 25 km (Kurashimo

et al. 1996; Kulinich and Valitov 2011). The lower Vp than the surrounding basins suggests that the rise is an extended, isolated continental crust (Kurashimo et al. 1996; Sato et al. 2018).

Revealing the lithospheric thickness, which is the first-order feature of the lithosphere structure, also benefits for better understanding the tectonics. Surface wave analyses have played that role for the Sea of Japan. The early studies by Abe and Kanamori (1970) and Evans et al. (1978) have estimated the averaged lithospheric thickness beneath the Sea of Japan to be ~ 30–40 km, using a few propagation paths crossing the Sea of Japan. Modern surface wave tomography analyses with teleseismic sources (Yoshizawa et al. 2010) and ambient noise (Zheng et al. 2011) have constructed 3D S-wave velocity (Vs) models beneath the Sea of Japan. Both models identify a higher velocity of the lithosphere and a lower velocity of the asthenosphere with the transition occurring at ~ 50–70 km depth. However, the limited spatial resolution prohibits the precise determination of the lithosphere–asthenosphere boundary (LAB) depth, which is inherent to surface wave studies.

The S-receiver function (S-RF) analysis (e.g., Yuan et al. 2006) can reveal lithospheric thicknesses at a high spatial resolution by detecting Sp converted phases at the LAB. The method is advantageous over P-receiver functions since the Sp converted phases are free from interferences by free-surface multiples. Because of its promised feature, numerous studies have employed this method to detect LAB (Kumar et al. 2005; Rychert et al. 2005; Lekic et al. 2011; Zhang et al. 2014; Hopper et al. 2020), and some of them have applied the method to the ocean-bottom environment (Kawakatsu et al. 2009; Kumar et al. 2011; Rychert et al. 2018, 2021; Mark et al. 2021). However, the effects of unconsolidated sediments at the ocean bottom on S-RF waveforms have not been fully understood yet, which is another focus of this paper.

This study aims to constrain the LAB depths by applying the S-RF method to seven ocean-bottom seismometers (OBSs) deployed at the Japan and Yamato Basins and the Yamato Rise. We perform transdimensional inversion to interpret S-RFs as Vs structure for three selected stations with good quality. Results indicate a thin lithosphere beneath the basins and a thick lithosphere beneath the Yamato Rise. Based on these results, we discuss the evolution process of the Sea of Japan.

Data

This study uses seismic waveform data from OBSs deployed at seven sites at the Sea of Japan: JS2, YMB3, and YMB4 located at the Yamato Basin; JPB4, JPB5, and JPB6 at the Japan Basin; and JS4 at the Yamato Rise (Fig. 1). The observation periods differ from place to place. The intended observation period was one year or more for each site, but instrument malfunction limits the data lengths for JPB5 and JS2 to less than one year. The longest observation period is about 2 years. Table 1 summarizes the observation data analyzed by this study.

All seismometers mentioned above contain Guralp CMG-3T broadband sensors (Güralp Systems Ltd.) with a flat response at periods shorter than 360 s. Additionally, the series of temporary seismic observations involve deployments of short-period OBSs with a natural frequency of 1 Hz. Unfortunately, these short-period sensors prove to be ineffective in detecting clear onsets on teleseismic S waveforms. Thus, the present study only focuses on the data from the broadband OBSs. The orientations of horizontal sensors are unknown because OBSs descend freely to the ocean bottom by gravity. The sensor orientations are estimated using the particle motion of Rayleigh waves (Stachnik et al. 2012). Horizontality of these sensors is maintained by gimbal.

S-receiver functions

A seismically noisy environment in the ocean requires a visual inspection of the waveforms. S waveforms from teleseismic events with $M > 5.5$ and epicentral distances of 55–85° undergo this visual inspection. Throughout this inspection, we consistently used a bandpass filter of 0.03–0.1 Hz to exclude the primary and secondary microseism bands and selected waveforms with clear onsets on the radial and vertical components. The bandpass filter used here does not affect the following receiver function calculation because of the cancelation by deconvolution. Figure 2 shows examples of S waveforms selected by this inspection. Out of 1218 waveforms, 216 waveforms successfully passed this inspection.

For these selected waveforms, S-RFs are calculated by deconvolving the radial component from the vertical component. We use a spectral division with a damping factor for the deconvolution and apply a low-pass filter to the deconvolution results:

Table 1 Summary of observation

Site name	Tectonic domain	Data availability
JPB4	Japan Basin	2017/07/18–2019/07/27
JPB5	Japan Basin	2018/07/25–2018/10/17
JPB6	Japan Basin	2017/07/18–2019/07/27
YMB3	Yamato Basin	2013/10/18–2015/8/11
YMB4	Yamato Basin	2013/10/18–2014/08/03, 2015/08/11–2016/08/08
JS2	Yamato Basin	2003/08/14–2003/11/15
JS4	Yamato Rise	2002/12/01–2003/11/15

$$SRF(t) = \frac{1}{\sqrt{2\pi}} \int_{-\infty}^{\infty} \frac{U_Z(\omega)U_R^*(\omega)}{U_R(\omega)U_R^*(\omega)+N_R(\omega)N_R^*(\omega)} LPF(\omega)\exp(i\omega t)d\omega, \quad (1)$$

where $SRF(t)$ represents the time series of S-RF; $U_Z(\omega)$ and $U_R(\omega)$ represent vertical and radial-component records in the frequency domain, respectively; $N_R(\omega)$ represents a pre-signal record on the radial component (i.e., noise contribution); and the asterisk signifies complex conjugate. The low-pass filter, $LPF(\omega)$, is given by

$$LPF(\omega) = \frac{1}{\sqrt{2}a} \exp\left(-\frac{\omega^2}{4a^2}\right). \quad (2)$$

Here, the factor a determines the cutoff frequency, which is set to 0.8 (i.e., 10% gain at ~ 0.4 Hz). The normalization constant $(1/\sqrt{2}a)$ compensates for energy loss due to filtering, depending on the definition of the Fourier transform. Time windows for the deconvolution start and end 50 s before and 150 s after the direct S arrival, respectively. After the deconvolution, resultant S-RFs undergo time- and polarity reversal for visualization purposes.

For further selecting S-RFs of good quality, we examine the waveform similarity between S-RFs from different teleseismic events. For each station, we calculate cross-correlation coefficients (CCs) between all S-RF pairs and retain S-RFs that show moderately high-similarity ($CC > 0.35$) to more than half of all data. We find that this thresholding effectively rejects S-RFs with anomalous features, such as the base-line drift or high-frequency oscillation, especially for stations JPB4, JS4, and YMB3 (Fig. 3). Unfortunately, we were not able to retain adequate numbers of data for the other stations, which is due to short observation periods or high noise levels. For the three successful stations, we stacked the selected S-RFs and use the stacked waveform as the input data for the subsequent inversion analysis (Fig. 3, green lines).

Transdimensional inversion

To constrain the parameters of seismic velocity models, we perform transdimensional inversion of an S-RF waveform. This inversion method uses a reversible-jump Markov-chain Monte Carlo (RJMCMC) algorithm (Green 1995) that allows the number of unknowns to be unknown. The algorithm automatically determines the number of unknowns in a balance between the data fit and parsimony. This feature can reduce the subjectivity of the model parameter choice. For RF inversion, it can eliminate the subjective choice of the layer number. Many RF studies have used the RJMCMC algorithm for inverse problems in recent years (Piana Agostinetti and Malinverno 2010,2018; Akuhara et al. 2020). Some of them have performed joint inversion with surface wave dispersion curves (Bodin et al. 2012; Calò et al. 2016), whereas detailed inversion settings differ among studies. The following sections elaborate on specific setting in this study. Notably, one can reproduce the inversion setting of this paper using a computer program package, SEIS_FILO (Akuhara 2021).

The goal of the RJMCMC algorithm is to sample the posterior probability distribution of the model

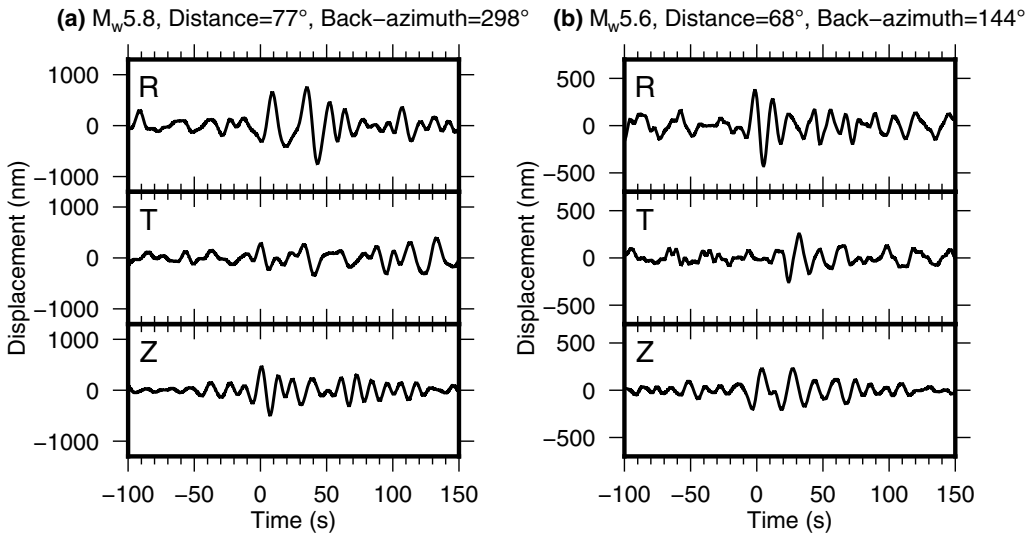

Fig. 2 Examples of teleseismic S waveforms recorded by a broadband ocean-bottom seismometer, YMB3 station. The waveforms are bandpass-filtered between 0.03 and 0.1 Hz. Zero on the time axis corresponds to the theoretical S arrivals. The magnitude, epicentral distance, and back-azimuth of the corresponding event are shown at the top

parameters ($\boldsymbol{m}_k$) and the hyperparameter (k) under a condition of a given data vector ($\boldsymbol{d}$). Here, the model parameter vector $\boldsymbol{m}_k$ has a variable dimension, which is a function of the hyperparameter k. According to Bayes' theorem, the posterior probability can be expressed as the product of a prior probability and a likelihood:

$$P(k, \boldsymbol{m}_k|\boldsymbol{d}) = D \cdot P(k, \boldsymbol{m}_k)P(\boldsymbol{d}|k, \boldsymbol{m}_k), \tag{3}$$

where $P(k, \boldsymbol{m}_k|\boldsymbol{d})$ is the posterior probability, $P(k, \boldsymbol{m}_k)$ is the prior probability, $P(\boldsymbol{d}|k, \boldsymbol{m}_k)$ is the likelihood, and D is a normalization constant. For RF inversion, prior probability reflects our knowledge on subsurface structures, and likelihood indicates the goodness of waveform fit. Ambiguity in D hampers the direct calculation of the posterior probability using Eq. 3. Instead, RJMCMC can simulate the probability through a random walk and a birth–death scheme.

Model parameters

We parameterize subsurface structure using the following hyperparameter and model parameters: the number of layers (k), Vs perturbation of each layer ($\delta\beta_i, i = 1 \cdots k$), and layer interface depths ($z_i, i = 1 \cdots k-1$). The velocity perturbation represents the difference from a reference velocity model. This reference model has smooth, increasing Vp and Vs with depth (Fig. 4), which we manually made by referring to established Vp models from previous seismic surveys (Sato et al. 2004, 2018; Nakahigashi et al. 2013) and an empirical Vp–Vs relation (Brocher 2005). With a given set of parameters (k, $\delta\beta_{1\cdots k}$, and $z_{1\cdots k-1}$), a layered, non-smoothed velocity model is constructed by first extracting Vp and Vs from the reference model at the center depth of each layer and then adding Vs perturbation to the extracted value. Vp is fixed at the extracted value without perturbation, and density is

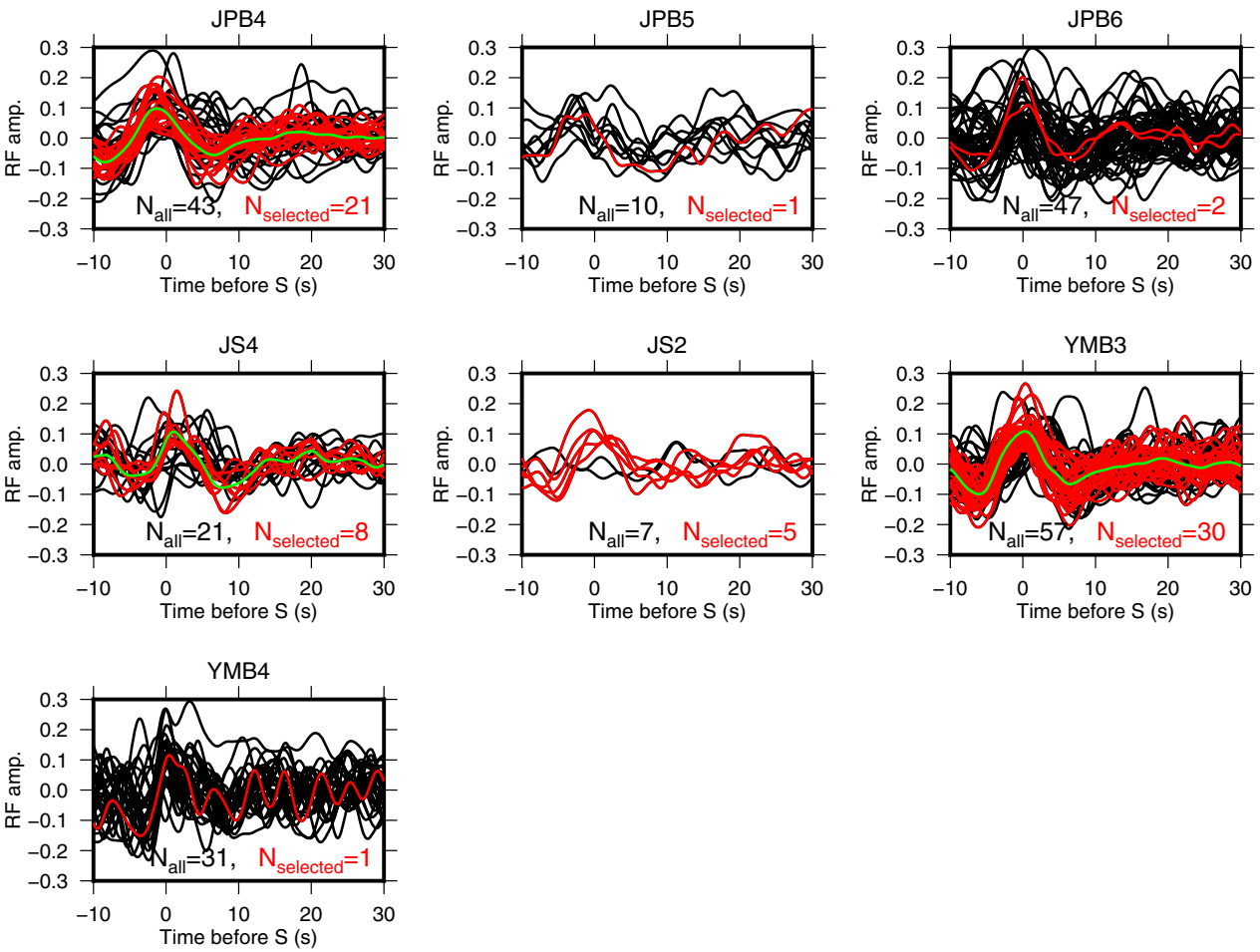

Fig. 3 S-receiver functions for each site. Black, red, and green traces represent rejected, accepted, and stacked receiver functions, respectively

scaled to Vp with an empirical relation (Brocher 2005). This treatment to Vp and Vs allows a Vp/Vs ratio to vary rather freely. Although the present study does not focus on the structure of Vp/Vs ratio due to its low sensitivity, we found that the resulting Vp/Vs ratios are mostly within an acceptable range (1.6–1.8) at the mantle depths. For the seawater, the acoustic velocity and density are assumed to be 1.5 km/s and 1.0 g/cm^3, respectively.

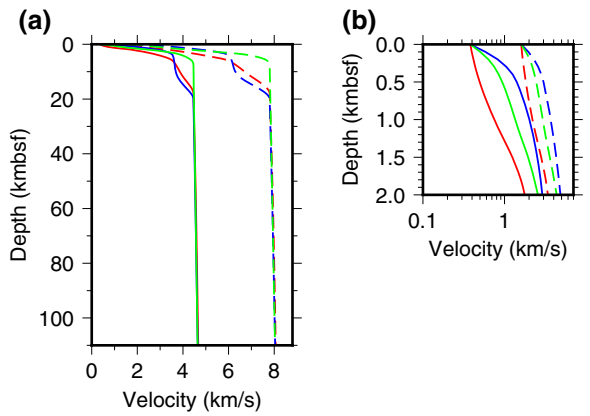

Fig. 4 Reference velocity models. Red, blue, and green lines represent the reference models for YMB3, JS4, and JPB4, respectively. Solid lines represent the S-wave velocity. Dashed lines represent the P-wave velocity. **a** Overall view. **b** Enlarged view for the shallow portion

Prior probability

Assuming independence of model parameters, the prior probability, $P(k, \boldsymbol{m}_k)$, may be expressed as

$$P(k, \boldsymbol{m}_k) = P(k)P(z_1, \cdots, z_k|k)P\left(\delta\beta_1, \cdots, \delta\beta_{k+1}|k\right). \tag{4}$$

We assume a truncated uniform prior for the number of layers (k), which is expressed as:

$$P(k) = \begin{cases} \frac{1}{k_{\max} - k_{\min}}, & k_{\min} \leq k < k_{\max} \\ 0, & \text{else} \end{cases}. \tag{5}$$

$k_{\min}$ and $k_{\max}$ are set to 1 and 31, respectively, throughout this study. We also use a non-informative prior for interface depths, which is given by

$$P(z_1, \cdots, z_k|k) = \begin{cases} \frac{k!}{(z_{\max} - z_{\min})^k}, & z_{\min} \leq z_i \leq z_{\max} \text{ for all } i = 1, \cdots, k \\ 0, & \text{else} \end{cases}. \tag{6}$$

Equation 6 corresponds to the Dirichlet distribution, which assumes that the layer interfaces are uniformly distributed over the range from $z_{\min}$ to $z_{\max}$ (Dosso et al. 2014). We set $z_{\min}$ and $z_{\max}$ to the sea depth and to 110 km, respectively.

For Vs perturbations, we use Gaussian distribution with a zero mean:

$$P\left(\delta\beta_1 \cdots \delta\beta_{k+1}|k\right) = \prod_{i=1}^{k+1} \frac{1}{\sqrt{2\pi\sigma_{\delta\beta}^2}} \exp\left(-\frac{\delta\beta_i^2}{2\sigma_{\delta\beta}^2}\right), \tag{7}$$

where the standard deviation, $\sigma_{\delta\beta}$, reflects the reliability of the reference velocity model. We set $\sigma_{\delta\beta}$ to 0.4 km/s.

Likelihood

We use a multivariate Gaussian distribution to formulate the likelihood:

$$P(\mathbf{d}|k, \mathbf{m}_k) = \frac{1}{\sqrt{(2\pi)^N |\mathbf{C}|}} exp\left[-\frac{1}{2}\left\{\mathbf{g}(k, \mathbf{m}_k) - \mathbf{d}\right\}^{\mathrm{T}} \mathbf{C}^{-1} \left\{\mathbf{g}(k, \mathbf{m}_k) - \mathbf{d}\right\}\right]. \tag{8}$$

Here, $\mathbf{C}$ is a covariance matrix and $\mathbf{g}(k, \mathbf{m}_k)$ is a synthetic S-RF. The covariance matrix is formulated as $C_{ij} = \sigma^2 r^{(j-i)^2}$, where σ is the standard deviation of the data noise and r is the temporal correlation (Bodin et al. 2012). We fix σ at the time-averaged value of the RF standard error obtained through the stacking process. We associate the temporal correlation with the Gaussian low-pass filter via $r = \exp(-(a\Delta t/2)^2)$, where Δt represents the sampling interval. The Gaussian parameter, a, is set to 0.8 as adopted for observed data.

A synthetic S-RF $\mathbf{g}(k, \mathbf{m}_k)$ is computed by the propagator matrix method (Thomson 1950). The method allows us to fully consider the reverberated phases, even with a water layer. The earth-flattening transformation is employed to account for the curvature of the Earth. The calculated radial and vertical component seismograms are converted into S-RFs through deconvolution, low-pass filtering, and time- and polarity reversal. For this deconvolution, we use a water-level damping with a factor of 0.001 (e.g., Clayton and Wiggins 1976). Here, the implemented deconvolution technique differs from what we use for the observation data for easy implementation.

Probabilistic sampling by reversible-jump Markov-chain Monte Carlo

The RJMCMC iteratively explores a transdimensional model space through a random walk and a birth–death scheme. At every iteration, the RJMCMC proposes a new model ($\boldsymbol{m}'_{k'}$) by modifying the model from the previous iteration ($\boldsymbol{m}_k$). This modification includes adding a layer (a birth proposal; $k' = k + 1$), removing a layer (a death proposal; $k' = k - 1$), moving a layer

interface ($z_i' = z_i + \varepsilon_z$), and perturbing Vs of a layer $\left(\delta\beta_i' = \delta\beta_i + \varepsilon_{\delta\beta}\right)$. The amount of modification, ε_z and $\varepsilon_{\delta\beta}$, is extracted from a Gaussian distribution with a zero mean and a standard deviation of 0.5 km and 0.2 km/s, respectively. Adding the k' th layer requires setting properties of the new layer (i.e., $z_{k'}$ and $\delta\beta_{k'}$). These properties are randomly determined using the same probability distribution as the prior probability (Dosso et al. 2014).

After the proposal, the RJMCMC judges a proposed model to be accepted or not using a Metropolis–Hastings-Green criterion (Green 1995; see Appendix 1). If the model is accepted, the accepted model is used in the next iteration to further make a new proposal. Otherwise, the previous model is held and used in the next iteration for a proposal. We perform 1,000,000 iterations, but the first 500,000 iterations are discarded to avoid dependency on the initial state (so-called burn-in period). After this burn-in period, we save models at every 500th iterations to simulate the posterior probability distribution. We run 100 mutually interacted Markov chains using a parallel tempering technique, which offers a more effective way of exploring a multidimensional space (Sambridge 2014; see Appendix 1).

Results and interpretation

Each inverted velocity structure shows a velocity decrease at the mantle depth, and the depths vary among sites (Figs. 5, 6, 7). We interpret these velocity decreases as the LAB, a boundary between the high-velocity lithosphere and low-velocity asthenosphere. By referring to the marginal probability distribution, we qualitatively define the LAB depths as depths where the velocity starts decreasing, which follows 45 km depth beneath the Yamato Basin (station YMB3) and Japan Basin (station JPB4) and 70 km depth beneath the Yamato Rise (station JS4).

The results also provide insights into the crustal thickness. The station YMB3 and JPB4 exhibit evident velocity discontinuities at ~ 20 km and ~ 10 km depth, respectively. These discontinuities are most likely to represent the Moho. The thicker crust obtained beneath the Yamato Basin agrees with previous seismic surveys (Hirata et al. 1989; Sato et al. 2006, 2018; Nakahigashi et al. 2013). No sharp velocity discontinuity, potentially corresponding to the Moho, is observed for station JS4. Instead, the velocity gradually increases to 30 km of depth, and we observe no velocity increase below the depth. This result only implies that the Moho beneath the Yamato Rise would not be deeper than 30 km but roughly agrees with previous studies (Kurashimo et al. 1996; Kulinich and Valitov 2011).

Notably, all results indicate an extremely low Vs (< 1 km/s) immediately beneath the seafloor, most likely reflecting water-saturated sediments. According to laboratory measurements, such slow velocities seem natural for water-saturated marine sediments (Hamilton 1979; Bowles 1997). Most seismic studies have rarely

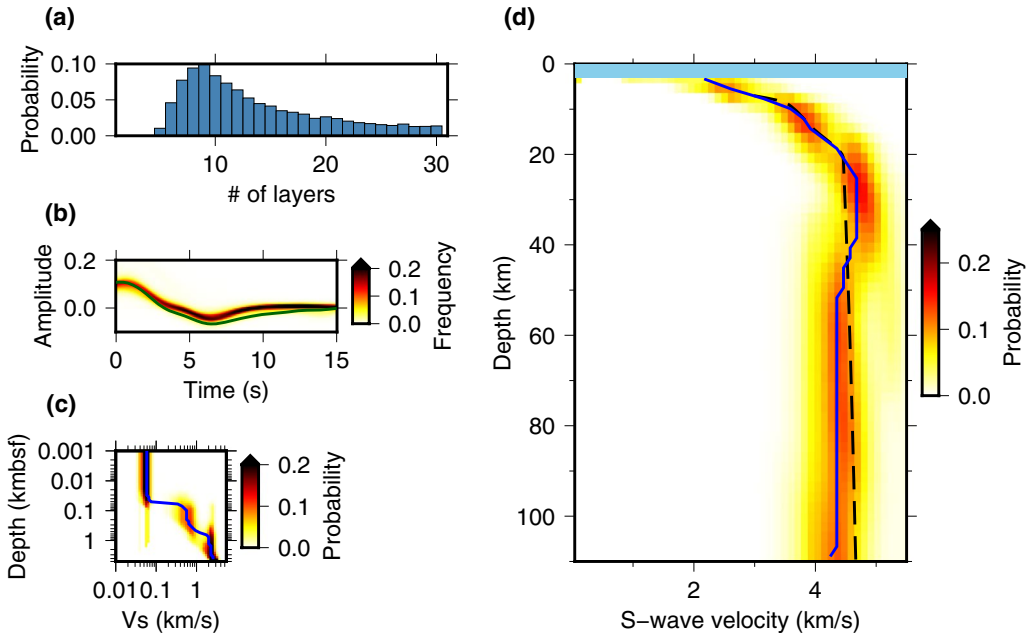

Fig. 5 Inversion results for station YMB3 located at the Yamato Basin. **a** Posterior probability of the number of layers. **b** Frequency distribution of predicted S-receiver functions. The background color shows the distribution, and the green line denotes the observed S-receiver function. **c**, **d** Posterior marginal probability of the S-wave velocity at each depth bin: **c** enlarged view for the seafloor sediment; **d** overall view. The background color shows the probability. Blue solid and black dashed lines denote the median and reference models, respectively

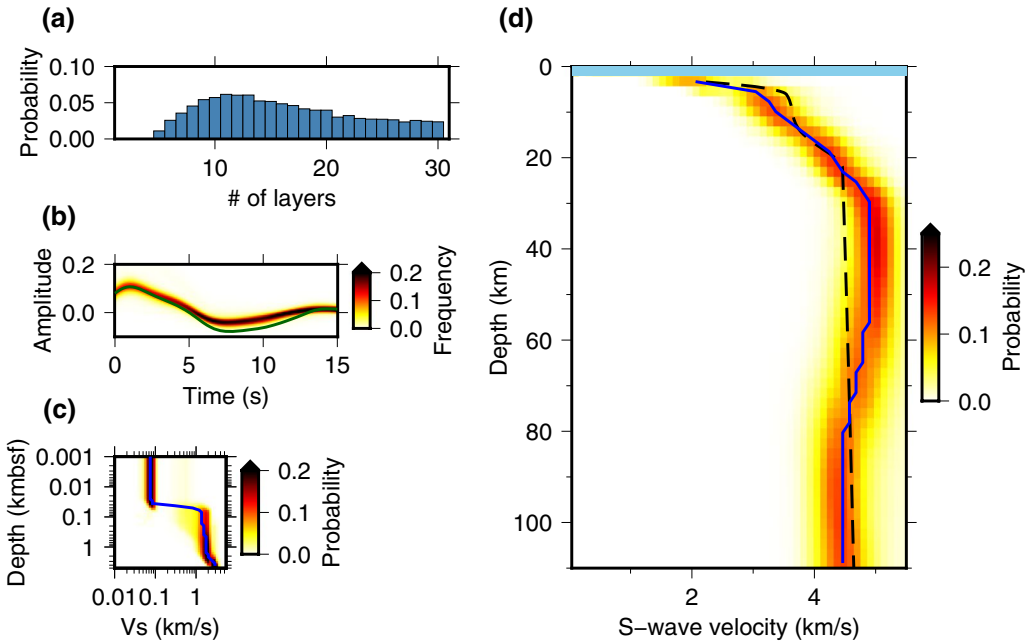

Fig. 6 The same as Fig. 5 but for station JS4 located at the Yamato Rise

considered low-velocity sediments when they focus on mantle structures. However, we found that the low velocity is necessary and should not be ignored to explain overall reduced amplitudes in observed waveforms. We will provide further discussion for this statement in the following section. Below this layer, we obtain relatively higher velocities but still lower than 1.0 km/s. Further below, there exist layers with Vs > 1 km/s, which we considered as the crust.

We acknowledge that the sampled models underestimate the amplitudes of the negative peak seen in the observation. This underestimation can result from

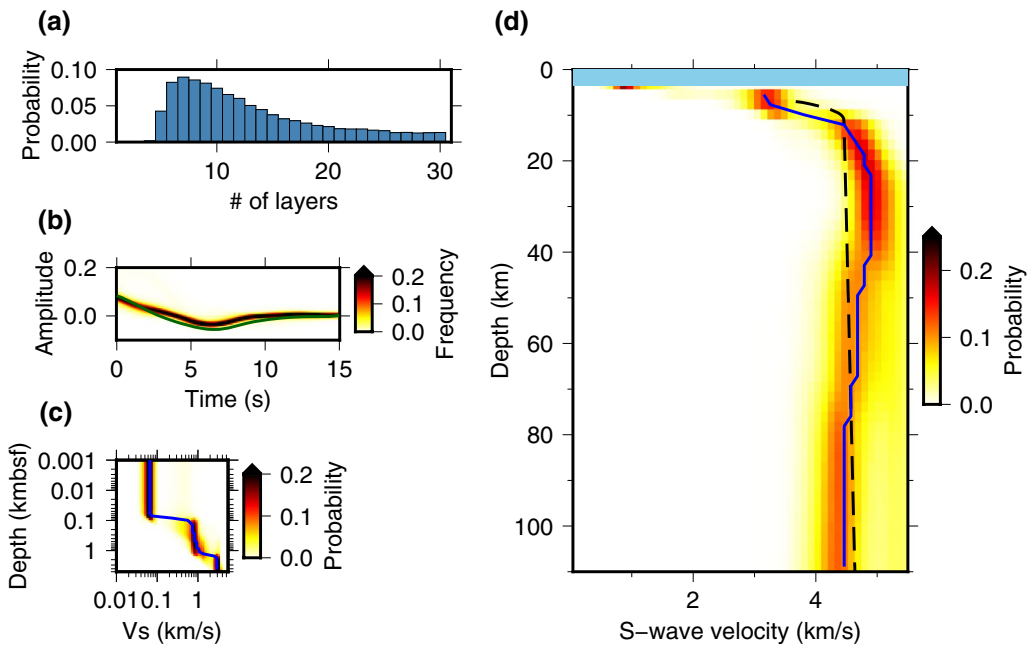

Fig. 7 The same as Fig. 5 but for station JPB4 located at the Japan Basin

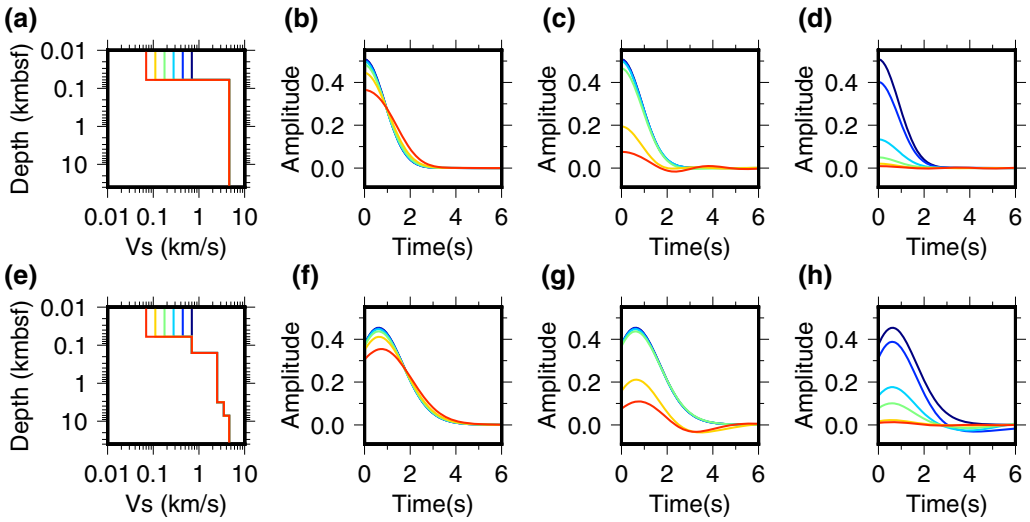

Fig. 8 Forward model experiments with **a**–**d** simple and **e**–**h** more realistic velocity models. **a**, **e** S-wave velocity (Vs) models tested through forward modeling. The models have an additional water layer with a 3-km thickness, although not shown in these panels. **b**–**d**, **f**–**h** Synthetic S-receiver functions calculated through different damping: **b**, **f** without damping, **c**, **g** with a damping factor of 0.001, and **d**, **h** with a damping factor of 0.01. Line colors correspond to those in **a** and **e**

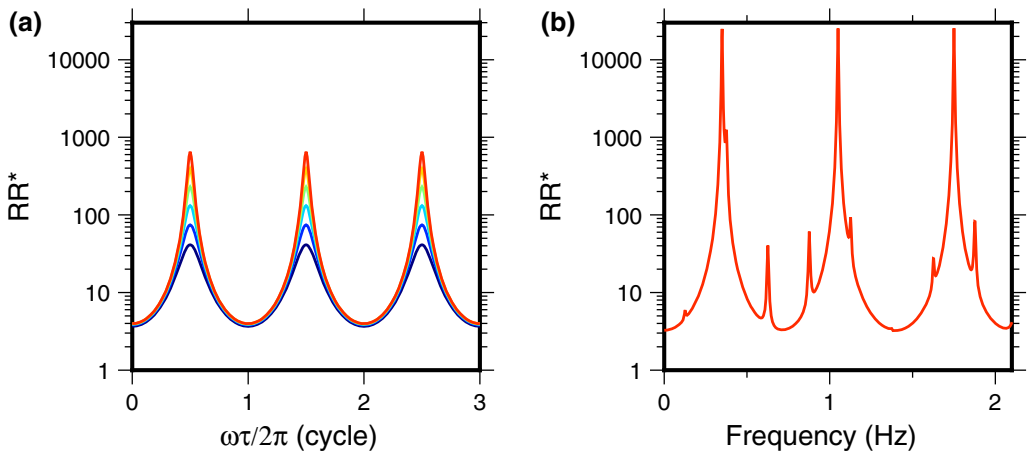

Fig. 9 Radial-component responses of a sediment layer overriding a half space. **a** Algebraic expression given by Equation 18. Color notation is the same as Fig. 8a. **b** Numerical results. The velocity model shown by the red line in Fig. 8a is used. The incident plane S-wave has a ray parameter of 0.11 s/km and a unit amplitude

deconvolution. A damping factor stabilizing the deconvolution suppresses S-RF amplitudes under the presence of low-velocity sediments, which will be discussed in detail in the following section. Other possible causes of this underestimation are lateral heterogeneity, including dipping layer interfaces and anisotropy because they can enhance the amplitude of Sp converted phases. Ideally, such effects will average out after stacking S-RFs from a wide back-azimuthal range. In our dataset, however, the enhanced signal, if exists, would remain even after the stacking because of unevenly distributed teleseismic events mostly from the Tonga-Kermadec subduction zone. Whatever the cause, this amplitude underestimation could distort the estimations of the velocity contrast at the LAB. The LAB depths would be less susceptive to this effect because the predicted waveforms explain the peak locations well.

Discussion

Contribution of sediment to S-receiver functions

Though not the center of focus, our inversion analysis has predicted thin, low-velocity layers at the top of the resulting models. This prediction may seem peculiar because low-frequency waveforms (< 0.1 Hz) are usually insensitive to thin layers. Another peculiarity lies in the considerably small amplitudes of the observed S-RFs, which are ~ 20% of the ordinary expectation. Understanding these peculiarities seems essential to appreciate our inversion results. The following paragraphs provide a unified explanation for these features, where spectral notches caused by sediment reverberations play a role. The sediment reverberations are inherent in ocean environments. Thus, insights presented here will be suited to other offshore S-RF studies.

Consider simple structure models consisting of water, sediment, and mantle layers, with varying sediment Vs (Fig. 8a). Synthetic S-RFs by the propagator matrix method and the water-level deconvolution exhibit decreasing amplitudes with an increasing velocity contrast at the sediment–mantle interface. The degree of this suppression depends on a damping factor imposed on the deconvolution (Fig. 8b–d). Without damping, where the amplitude reduction mostly reflects a magnified S-to-S transmission coefficient at the interface, we only obtain a slight peak reduction to ~0.35 even for the extreme case (Fig. 8b). This trivial reduction (~30%) is insufficient to explain the observed amplitude reduction (~80%). A damping factor added to a deconvolution denominator exerts a more significant control over the S-RF amplitudes and allows the reproduction of the observed peak amplitudes (Fig. 8c, d). This tendency still holds even if we employ more complex, realistic velocity models (Table 2; Fig. 8e–h).

Algebraic formulation of the reverberation phases offers further insight into the damping effects. Assume a simple water–sediment–mantle model (Fig. 8a) and a vertical incidence of a teleseismic S waveform to the model. The power spectrum of the radial-component response, given by Equation 18 in Appendix 2, has spectral notches, and the notch depths increase with an increasing velocity contrast at the interface (Fig. 9a). At a higher velocity contrast, such "deep" notches are more likely subjected to damping effects. For the observation data, high-level noise can also fill in these notches. Such a spectral fill in will increase the denominator of deconvolution and, thus, reduce S-RF amplitudes. Figure 9b confirms this situation through a numerical calculation using the propagator matrix method, which considers an oblique incidence of a waveform and includes secondary effects such as P-to-S conversions and the sea water layer. The resultant spectrum still indicates similar spectral notches to algebraic ones.

The above discussion implies a tradeoff between the sediment Vs and the damping value. Our arbitral selection of the damping factor during inversion possibly biases the estimated sediment Vs (and their thicknesses), but we found that this choice does not affect LAB depths drastically. We acknowledge that we employed different damping schemes for the observed and synthetic S-RF calculations (frequency-dependent damping vs. constant water-level damping). Effects from various damping schemes should be investigated in the future. Alternatively, deconvolution may be avoided using transfer function-based techniques (Bodin et al. 2014; Frederiksen and Delaney 2015; Akuhara et al. 2019). We note that a well-known velocity–thickness tradeoff is mitigated during the inversion, as indicated by Figs. 5c, 6c, 7c, due to the amplitude sensitivity to the velocity discussed above.

In recent years, many studies have directed their efforts toward constraining the seismic properties of the seafloor sediment from teleseismic P waveforms to decipher deeper structures (Akuhara et al. 2017; Agius et al. 2018; Tonegawa et al. 2019; Zhang and Olugboji 2021). The later Ps phases from deeper seismic discontinuities are potentially masked by reverberations due to the sediment, and thus predicting the timing of these reverberations is essential. Unfortunately, such attempts are often challenging due to fine-scale (~ 100 m) layered structures within the sediment (Akuhara et al. 2019). Even transdimensional approach, where prior knowledge on the sediment is not necessary, has been reported to misinterpret sediment reverberations as an indicator of spurious low-velocity zones when inverting P receiver functions jointly with lower-frequency surface wave dispersion curves (Gao et al. 2019). The presented transdimensional inversion of S-RFs has a distinct advantage in that the time window of interest does not include shallow reverberations arriving earlier than the direct S arrival. Further investigation of the damping effects would establish this method as a more promising tool.

Table 2 Velocity models used in forward modeling

	Vp (km/s)	Vs (km/s)	Density (g/cm^3)	Thickness (km)
Seawater	1.5	–	1.0	3
Sediment #1	1.5	0.07–0.7	1.3–1.9	0.05
Sediment #2	2.1	0.7	1.9	0.1
Crust #1	4.3	2.5	2.4	3
Crust #2	6.0	3.5	2.7	4
Mantle	8.1	4.6	3.3	–

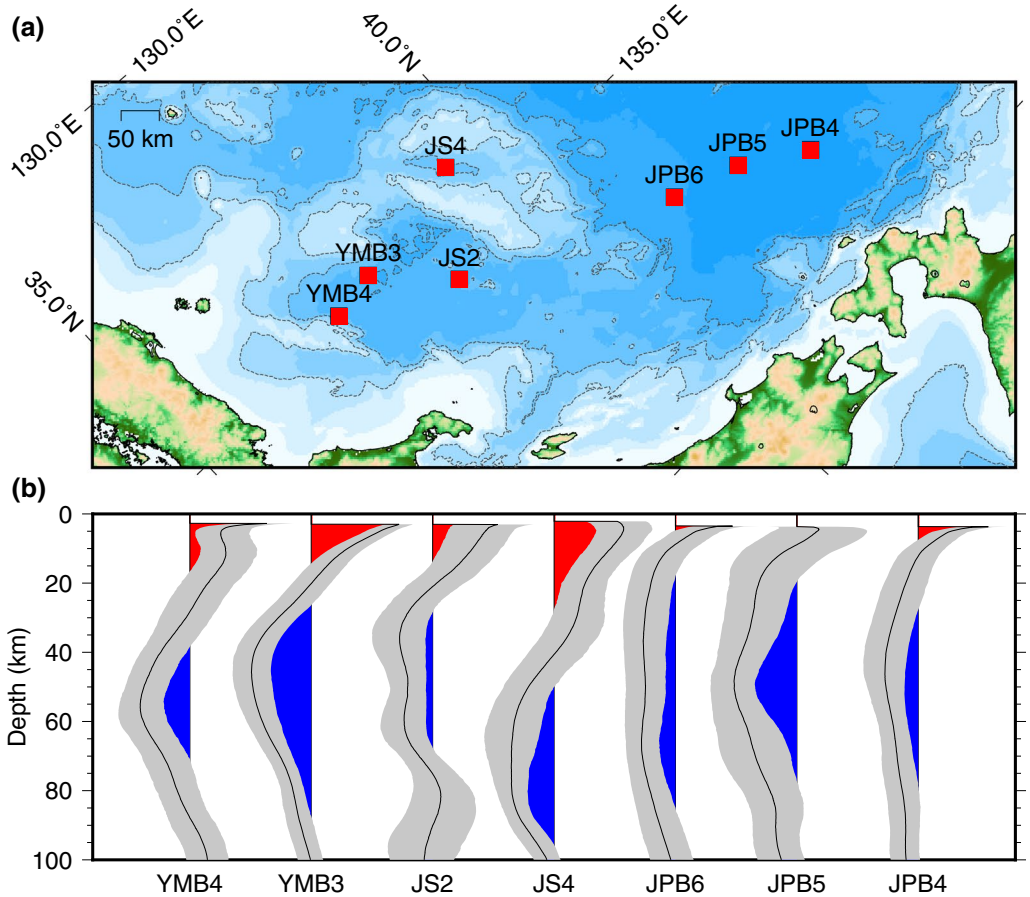

Fig. 10 Time-to-depth-converted and stacked S-receiver functions (S-RFs) for each station. **a** Stations locations (red squares). **b** The depth-converted, stacked S-RFs. Positive and negative amplitudes are shaded in red and blue, respectively. The gray shade represents the 95% confidence interval from bootstrap resampling 1000 times

Lateral variation in lithospheric structure

We have performed the inversion analysis for three good-conditioned stations, and the results show the thickest lithosphere beneath the Yamato Rise. Here, we argue that S-RFs from the other stations qualitatively support this finding. Figure 10 shows a stack of time-to-depth-converted S-RFs at each station, including S-RFs rejected by the CC criteria. We converted time to depth using the three median models from the inversion results (Blue lines in Figs. 5, 6, 7), assuming a laterally homogeneous structure across each tectonic domain, i.e., we use the JPB4 model for migrating JPB4, JPB5, and JPB6 data; the YMB3 model for YMB3, YMB4, and JS2 data; and the JS4 model for JS4 data. All stacked receiver functions show a significant negative peak representing the LAB (Fig. 10b). The exact depths are hard to estimate from this stacking because of the broadened peak. Nevertheless, the results still imply the thickest lithosphere beneath the Yamato Rise and a relatively constant thickness beneath the surrounding basins.

An independent surface wave tomography study (Yoshizawa et al. 2010) also indicates the thickened lithosphere beneath the Yamato Rise (Fig. 11). Their model shows a high Vs zone at shallow mantle depths (30–60 km) beneath the Yamato Rise (Fig. 11b), and its lateral extent roughly corresponds to that of the topographic high (Fig. 11a). A strong velocity contrast resides around 60–80 km depth, which agrees with our inverted model. The contrast becomes relatively obscure further southward, beneath the Yamato Basin. Still, we see that the depth of the velocity contrast becomes shallower toward the Yamato Basin ($x = 200$–300 km, Fig. 11b), and that the depth roughly agrees with our estimated LAB depth (45 km beneath the YMB3). Further southward ($x < 100$ km), the image does not show a simple structure with a high-velocity lithosphere above and a low-velocity asthenosphere below. Moreover, the structure varies laterally. Such complexity may reflect a transition from the basin to the Japanese island-arc domains. A direct comparison of our results to the tomographic model seems

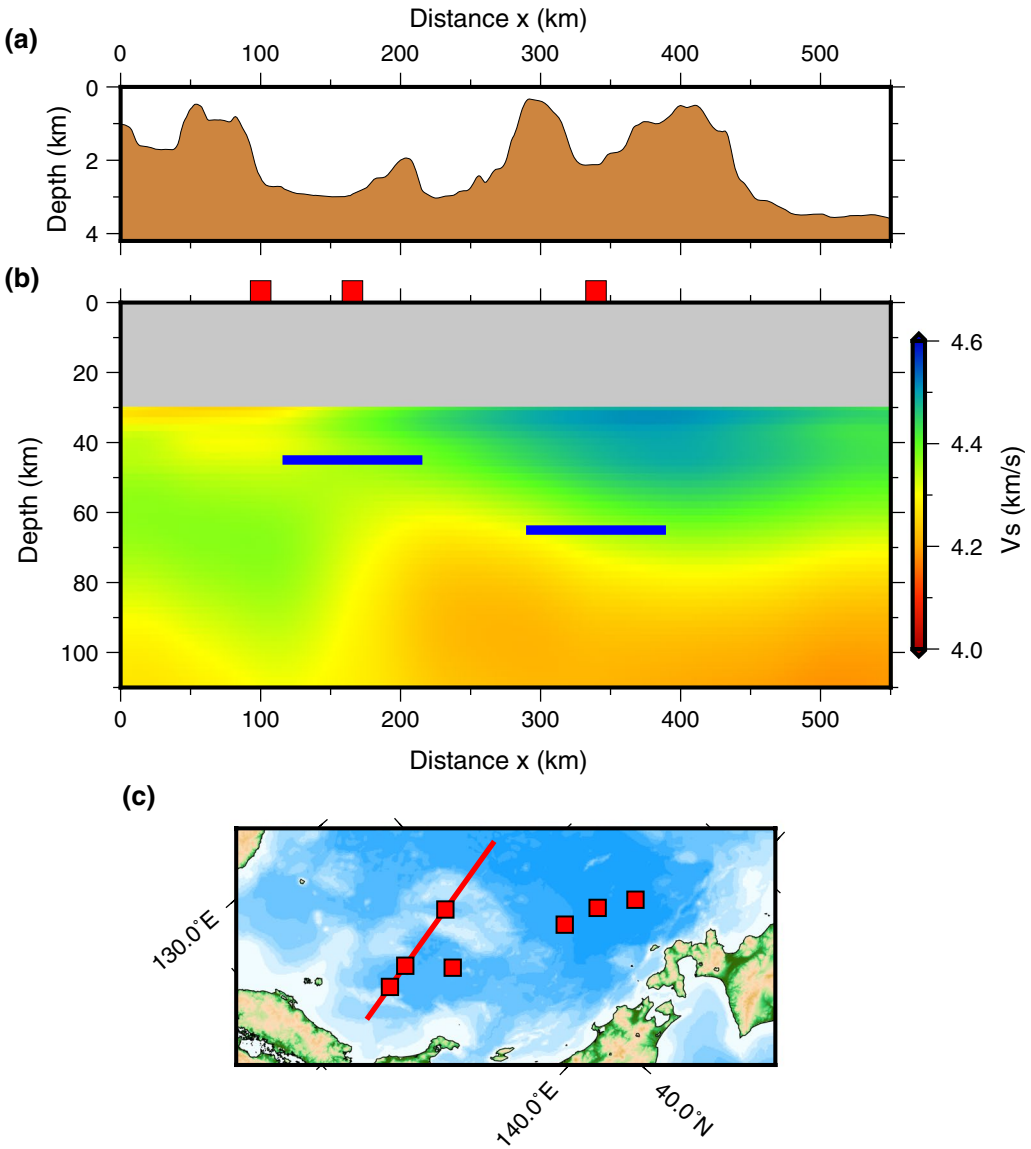

Fig. 11 Comparison to surface wave tomography model. **a** Seafloor topography profile. **b** Cross section of S-wave velocity model estimated by surface wave tomography (Yoshizawa et al. 2010). The shallow portion (< 30 km depth) is masked by the gray shade because of insufficient resolution with long-period surface waves. Blue horizons roughly indicate the lithosphere–asthenosphere boundary inferred from the inversion. Red squares denote station locations. **c** Profile location (red line) and station locations (red squares)

difficult for this portion due to the limited spatial resolution of the surface wave analysis.

The depth-converted S-RFs in Fig. 10 also offer implications on the crustal thickness. The first positive peak can represent the combination of S-to-P converted phases from the sediment–crust, intra-crust, and Moho discontinuities, and thus, its peak width will roughly correspond to the crustal thickness. Consequently, the results indicate the thickest crustal thickness beneath the Yamato Rise, moderate thicknesses beneath the Yamato Basin, and thin thicknesses beneath the Japan Basin. This first-order feature is consistent with active-source seismic surveys (Hirata et al. 1989; Sato et al. 2004, 2018,2020; Nakahigashi et al. 2013). Interestingly, the Yamato and Japan Basins seem to have comparable LAB depths, as suggested from inversion results. This similarity contrasts with the observed variation in crustal thicknesses. We further discuss this point in the subsequent section.

Tectonic implications

This study has identified the LAB beneath the Sea of Japan back-arc basin. Results have shown (1) thick

lithosphere beneath the Yamato Rise and (2) a comparable lithosphere thickness beneath the Yamato and Japan Basins. Whereas an ambient noise tomographic study has implied a similar feature (Zheng et al. 2011), our S-RF analysis has emphasized it through its high-resolution constraints. This section describes tectonic implications from the obtained first-order features of the lithosphere. Figure 12 schematically shows our interpretations.

Many studies assume that the Yamato Rise is a continental fragment isolated from the Asia continent (e.g., Tamaki 1985; Kurashimo et al. 1996). The crustal Vp has supported this hypothesis, which is lower than typical velocities for oceanic crusts (Sato et al. 2018). Tectonic reconstruction models suggest that the Yamato Rise lies adjacent to the Sikhote Alin at the pre-rift stage (Kim et al. 2007). In the vicinity, northeastern China, an S-RF study has identified the LAB at ~ 150 km depth (Zhang et al. 2014), which may roughly indicate the original lithosphere thickness beneath the Yamato Rise. Considering the current LAB depth ~ 70 km obtained by this study, the lithosphere may undergo lateral extension by a factor of ~ 2 through the rifting process. Such an extension can induce normal faulting in the crust and contribute to trough formation, which appears in the seafloor topography.

The origin of the Yamato Basin, which has an anomalously thick crust, is under debate. Some studies interpreted the crust as an extended continental crust (e.g., Nishizawa and Asada 1999; Nakahigashi et al. 2013), whereas others as a thickened oceanic crust (e.g., Hirata et al. 1989; Sato et al. 2018). In contrast, there is no doubt that the seafloor spreading is the origin of the Japan Basin, judging from the lineation pattern in the seafloor magnetic anomaly (Seama and Isezaki 1990). The estimated velocity structures with comparable LAB depths may imply that the Yamato Basin also originates from the seafloor spreading like the Japan Basin, assuming that the LAB depths primarily reflect the thermal state and thus depend on the age (Stein and Stein 1996; Kawakatsu et al. 2009; Schmerr 2012). Note that the two basins have similar ages of 19–20 Myr (Kaneoka et al. 1992). We argue that our estimated lithospheric thickness (~ 45 km) roughly agrees with observations from other ocean regions with similar lithospheric ages (Rychert et al. 2020 and references therein) and also with the prediction from a subsolidus model for the oceanic LAB (Karato et al. 2012). Our results do not exclude the possibility that the lithospheric extension has formed the Yamato Basin. However, if this true, there would be no anticipation that both basins show consistent thicknesses.

Our results imply the thicker crust beneath the Yamato Basin than beneath the Japan Basin, consistent with previous active seismic-source studies (Van Horne et al. 2017 and references therein). Hirata et al. (1989) has associated the thickened oceanic crust beneath the Yamato Basin with an abrupt tectonic reversal from extension to

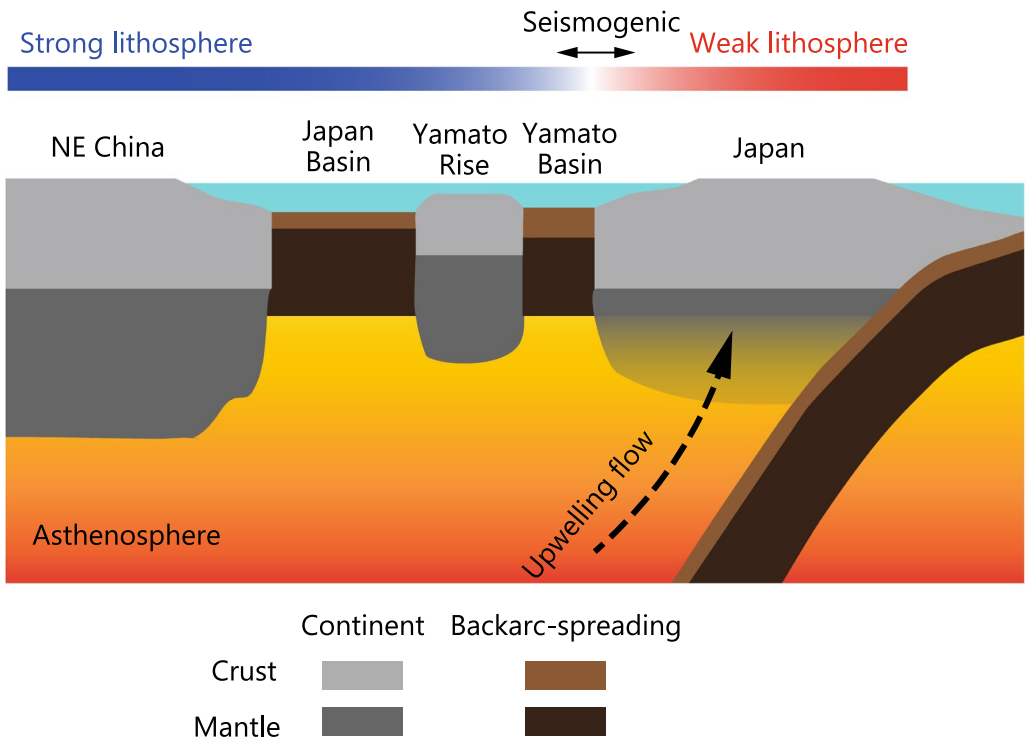

Fig. 12 Schematic illustration of the lithosphere–asthenosphere system across northeastern Japan, the Sea of Japan, and northeastern China

compression at 15 Ma (Sato, 1994): the compressional field prohibits a lateral growth of the crust but leads to a vertical growth instead. Such an abnormal event at 15 Ma could delay the lithosphere cooling process, which originally initiates at 19–20 Ma, but according to the global compilation of the oceanic LAB depths (Rychert et al. 2020), such a slight age difference (4–5 million years) would not cause an observable and systematic difference in LAB depths by far beyond ~ 10 km. Thus, we conclude that the comparable LAB depths and different crustal thicknesses between the Yamato and Japan Basins can coexist.

Whereas we have observed evident indicators of the LAB from S-to-P converted phases across a wide area of the Sea of Japan (Figs. 5, 6, 7 and 10), there is no observable LAB reported beneath the Japanese Islands. Mantle upwelling flow, related to volcanisms (Nakajima et al. 2001; Nakajima and Hasegawa 2007), can thermally or mechanically complicate structures at the depth and may obscure the clear LAB manifestation. The coherent Sp phase observed beneath the Sea of Japan suggests a mechanically strong lithosphere, whereas the lithosphere likely becomes weak beneath the Japanese Islands because of the volcanisms. Such contrast will be of importance for considering seismogenesis around Japan. For instance, a seismogenic belt in the eastern margin of the Sea of Japan, running sub-parallel to the Japanese Island (Fukao and Furumoto 1975), may be attributed to strain accumulated near the transition between the strong and weak lithosphere.

A limitation of this study lies in the sparse distribution of OBSs. So far, there has been no passive seismic monitoring conducted at the Tsushima Basin. Such observation would help gain further insights into the tectonics of the Sea of Japan. Owing to its similar crustal features to the Yamato Basin, identifying the LAB depth beneath the Tsushima Basin may (or may not) support our interpretation for the Yamato Basin. Additionally, the lithospheric thickness would be a key parameter to understanding regional tectonic deformation processes. Currently, southwestern Japan experiences a tectonic push by the subducting Philippine Plate, which increases the potential risk of inland earthquakes. The advanced insights into the lithospheric structure obtained for the Tsushima Basin and those for the Yamato Basin may lead to a better appreciation of such potential earthquake hazards.

Conclusions

This study investigated the lithospheric structure beneath the Sea of Japan through inversion of S-RF waveforms derived from the OBS data. Inverted structures show a velocity decrease in the mantle depths, and we conclude the LAB is located at ~ 45 km depth beneath the Japan and Yamato Basins and ~ 70 km beneath the Yamato Rise. The deepened LAB beneath the rise most likely reflects its continental origin, but the depth is still shallower than that beneath northeastern China, suggesting lithospheric extension. The obtained comparable LAB depths for the Japan and Yamato Basins indicate that both basins share a common tectonic origin: the back-arc spreading. The origin of the enigmatic Yamato Basin has been controversial, and many active-source seismic surveys have investigated shallow crustal structures for clues. This study offers an additional constraint, for the first time, from the deeper lithospheric structure, which owes to the high-resolution feature of receiver functions.

This study also discusses technical issues of S-RFs at the ocean bottom. As an explanation of observed abnormally reduced amplitudes, we propose a theoretical perspective on how sediment reverberations and additive damping (or noise) to the deconvolution denominator can reduce S-RF amplitudes. However, our treatment of this issue may not be sufficient, as implied by the systematic underestimation of S-RF amplitudes for deeper phases. This point should be further investigated in the future, which renders S-RF methods using OBS data a more promising tool to decipher the lithosphere–asthenosphere system.

Appendix 1: Acceptance criteria and parallel tempering

The RJMCMC algorithm aims to extract samples from model spaces such that samples follow their posterior probability. Each proposed model needs to be accepted or rejected under the equilibrium condition. For a fixed dimension (i.e., $k = constant$), this condition can be met by accepting proposed models with the probability given by the Metropolis–Hastings criterion:

$$\alpha_{MH}\left(k, \boldsymbol{m}_k^{'} | k, \boldsymbol{m}_k\right) = \min\left[1, \frac{P(k,\boldsymbol{m}')}{P(k,\boldsymbol{m})} \cdot \frac{P\left(\boldsymbol{d}|k,\boldsymbol{m}_k^{'}\right)}{P\left(\boldsymbol{d}|k,\boldsymbol{m}_k\right)} \cdot \frac{Q\left(\boldsymbol{m}_k|\boldsymbol{m}_k^{'}\right)}{Q\left(\boldsymbol{m}_k^{'}|\boldsymbol{m}_k\right)}\right]. \tag{9}$$

Here, $\boldsymbol{m}_k$ and $\boldsymbol{m}_k^{'}$ are the last-accepted and proposed models, respectively; and $Q(\boldsymbol{m}_k^{'}|\boldsymbol{m}_k)$ is the probability that a random walk from $\boldsymbol{m}_k$ to $\boldsymbol{m}_k^{'}$ occurs. Our setting simplifies Eq. 9 because of the symmetricity of a random walk (i.e., $Q\left(\boldsymbol{m}_k^{'}|\boldsymbol{m}_k\right) = Q(\boldsymbol{m}_k|\boldsymbol{m}'_k)$):

$$\alpha_{MH}\left(k, \boldsymbol{m}_k^{'}|k, \boldsymbol{m}_k\right) = \min\left[1, \frac{P(k,\boldsymbol{m}')}{P(k,\boldsymbol{m})} \cdot \frac{P\left(\boldsymbol{d}|k,\boldsymbol{m}_k^{'}\right)}{P\left(\boldsymbol{d}|k,\boldsymbol{m}_k\right)}\right]. \tag{10}$$

Equations 9 and 10 assume that the model space dimension does not change through a random walk. Green (1995) has introduced the Metropolis–Hastings–Green criterion that can account for the dimensional change:

$$\alpha_{MHG}\left(k', \boldsymbol{m}_{k'}^{'}|k, \boldsymbol{m}_k\right) = \min\left[1, \frac{P\left(k', \boldsymbol{m}_{k'}^{'}\right)}{P(k,\boldsymbol{m}_k)} \cdot \frac{P\left(\boldsymbol{d}|k', \boldsymbol{m}_{k'}^{'}\right)}{P\left(\boldsymbol{d}|k,\boldsymbol{m}_k\right)} \cdot \frac{Q\left(k,\boldsymbol{m}_k|k', \boldsymbol{m}_{k'}^{'}\right)}{Q\left(k', \boldsymbol{m}'_{k'}|k,\boldsymbol{m}_k\right)} \cdot |\boldsymbol{J}|\right]. \tag{11}$$

The Jacobian $|\boldsymbol{J}|$ in Eq. 11 adjusts unit volume change in the model space. Specific configurations of a random walk are known to cancel out similar terms in Eq. 11 (Dosso et al. 2014; Sen and Biswas 2017), leading to

$$\alpha_{MHG}\left(k', \boldsymbol{m}_{k'}^{'}|k, \boldsymbol{m}_k\right) = \min\left[1, \frac{P\left(\boldsymbol{d}|k', \boldsymbol{m}_{k'}^{'}\right)}{P\left(\boldsymbol{d}|k,\boldsymbol{m}_k\right)}\right]. \tag{12}$$

To enhance the efficiency of model sampling, the parallel tempering technique (Geyer and Thompson 1995; Sambridge 2014) introduces an additional parameter representing temperature (T_i) to Eqs. 10 and 12:

$$\alpha_{MH}\left(k, \boldsymbol{m}_k^{'}|k, \boldsymbol{m}_k\right) = \min\left[1, \frac{P(k,\boldsymbol{m}')}{P(k,\boldsymbol{m})} \cdot \left\{\frac{P\left(\boldsymbol{d}|k,\boldsymbol{m}_k^{'}\right)}{P\left(\boldsymbol{d}|k,\boldsymbol{m}_k\right)}\right\}^{\frac{1}{T_i}}\right] \tag{13}$$

and

$$\alpha_{MHG}\left(k', \boldsymbol{m}_{k'}^{'}|k, \boldsymbol{m}_k\right) = \min\left[1, \left\{\frac{P\left(\boldsymbol{d}|k', \boldsymbol{m}_{k'}^{'}\right)}{P\left(\boldsymbol{d}|k,\boldsymbol{m}_k\right)}\right\}^{\frac{1}{T_i}}\right]. \tag{14}$$

Higher temperatures than unity lose the acceptance criterion to accept more models. Such tempered chains can walk through the broader region in the model space consequently. However, this modification by T_i breaks the equilibrium condition, and thus the sampled model does not simulate the posterior probability distribution. The parallel tempering technique remedies this issue by running 100 MCMC chains with different temperature (T_i; $i = 1 \cdots 100$) in parallel. At each iteration, two chains are arbitrarily selected, and their temperatures are swapped with a probability of

$$\alpha_{PT}(i,j) = \min\left[1, \left\{\frac{P\left(\boldsymbol{d}|k^j, \boldsymbol{m}_{kj}^{j}\right)}{P\left(\boldsymbol{d}|k^i, \boldsymbol{m}_{ki}^{i}\right)}\right\}^{\frac{1}{T_i}} \left\{\frac{P\left(\boldsymbol{d}|k^i, \boldsymbol{m}_{ki}^{i}\right)}{P\left(\boldsymbol{d}|k^j, \boldsymbol{m}_{kj}^{j}\right)}\right\}^{\frac{1}{T_j}}\right], \tag{15}$$

where superscripts i, j represent the indices for MCMC chains. Equation 15 guarantees that this temperature swap meets the equilibrium condition. The posterior probability can be retrieved by gathering models accepted with non-tempered chains. Our inversion involves 20 chains having a unit temperature (i.e., non-tempered). For the other 80 chains, we randomly set temperatures, which range from 1 to 20.

Appendix 2: Algebraic expression for sediment reverberations

Let us consider the simple velocity model shown in Fig. 8a. When a plane, impulsive, unit amplitude, upgoing, nearly vertical SV waveform incidents to this structure model, a radial-component elastic response at the sediment top is approximately given by

$$u_r(t) = f_S \acute{S}\acute{S}\left[\sum_{n=0}^{\infty}\left(-\grave{S}\acute{S}\right)^n \delta(t - n\tau)\right], f_s = 2, \acute{S}\acute{S} = 1 + \grave{S}\acute{S}, \\ \tau = \frac{2h_1}{\beta_1}, \grave{S}\acute{S} = \frac{\rho_2\beta_2 - \rho_1\beta_1}{\rho_1\beta_1 + \rho_2\beta_2} \tag{16}$$

in the time domain and

$$U_R(\omega) = 2\left(1 + \grave{S}\acute{S}\right)\frac{1}{\left(1 + \grave{S}\acute{S}e^{-i\omega\tau}\right)} \tag{17}$$

in the frequency domain (e.g., Akuhara and Mochizuki 2015; Yu et al. 2015; Zhang and Olugboji 2021), where h_1, β_1, and ρ_1 represent a thickness, Vs, and a density of the overriding sediment layer, respectively; β_2 and ρ_2 represent Vs and a density of the half space; f_s represents free-surface reflection; τ represents a two-way travel time of S-wave passing through the sediment layer; and $\grave{S}\acute{S}$ and $\acute{S}\acute{S}$ represent reflection and transmission coefficients at the layer interface, respectively. From Eq. 17, we obtain the denominator of deconvolution without damping:

$$U_R(\omega)U_R^*(\omega) = \frac{2\left(1 + \grave{S}\acute{S}\right)^2}{1 + \grave{S}\acute{S}\cos(\tau\omega)}. \tag{18}$$

Acknowledgements
We thank Kazunori Yoshizawa for providing the tomography model of the Sea of Japan. We thank Vedran Lekić and an anonymous reviewer for their insightful comments.

Authors' contributions
TA analyzed waveform data. TA, KN, and MS interpreted the data and designed the seismic observation. All authors contribute to the data acquisition and read and approved the final manuscript.

Funding
This study was conducted as a part of Integrated Research Project on Seismic and Tsunami Hazards around the Sea of Japan by the Ministry of Education, Culture, Sports, Science, and Technology (MEXT) of Japan.

Availability of data and materials
The teleseismic waveforms analyzed during this study are available from the corresponding author on reasonable request.

Declarations

Competing interests
The authors declare no competing interests.

Author details
[1]Earthquake Research Institute, The University of Tokyo, 1-1-1, Yayoi, Bunkyo-ku, Tokyo 113-0032, Japan. [2]Department of Marine Resources and Energy, Tokyo University of Marine Science and Technology, 4-5-7, Konan, Minato-ku, Tokyo 108-8477, Japan. [3]Miyazaki Observatory, Research Center for Earthquake Prediction, Disaster Prevention Research Institute, Kyoto University, 3884, Kaeda, Miyazaki, Kyoto 889-2161, Japan. [4]National Research Institute for Earth Science and Disaster Resilience, 3-1, Tennodai, Tsukuba-shi, Ibaraki 305-0006, Japan.

Received: 12 May 2021 Accepted: 16 August 2021
Published online: 28 August 2021

References

Abe K, Kanamori H (1970) Mantle structure beneath the Japan Sea as revealed by surface waves. Bull Earthq Res Inst Univ Tokyo 48:1011–1021
Agius MR, Harmon N, Rychert CA et al (2018) Sediment characterization at the equatorial mid-atlantic ridge from P-to-S teleseismic phase conversions recorded on the PI-LAB experiment. Geophys Res Lett 45:12244–12252. https://doi.org/10.1029/2018GL080565
Akuhara T (2021) SEIS_FILO (v1.2.0). Zenodo. https://doi.org/10.5281/zenodo.4456184.
Akuhara T, Mochizuki K (2015) Hydrous state of the subducting Philippine Sea plate inferred from receiver function image using onshore and offshore data. J Geophys Res Solid Earth 120:8461–8477. https://doi.org/10.1002/2015JB012336
Akuhara T, Mochizuki K, Kawakatsu H, Takeuchi N (2017) A fluid-rich layer along the Nankai trough megathrust fault off the Kii Peninsula inferred from receiver function inversion. J Geophys Res Solid Earth 122:1–14. https://doi.org/10.1002/2017JB013965
Akuhara T, Bostock MG, Plourde AP, Shinohara M (2019) Beyond receiver functions: Green's function estimation by transdimensional inversion and its application to OBS data. J Geophys Res Solid Earth 124:1944–1961. https://doi.org/10.1029/2018JB016499
Akuhara T, Tsuji T, Tonegawa T (2020) Overpressured underthrust sediment in the nankai trough forearc inferred from transdimensional inversion of high-frequency teleseismic waveforms. Geophys Res Lett. https://doi.org/10.1029/2020GL088280
Bodin T, Sambridge M, Tkalćić H et al (2012) Transdimensional inversion of receiver functions and surface wave dispersion. J Geophys Res Solid Earth 117:1–24. https://doi.org/10.1029/2011JB008560
Bodin T, Yuan H, Romanowicz B (2014) Inversion of receiver functions without deconvolution—application to the Indian craton. Geophys J Int 196:1025–1033. https://doi.org/10.1093/gji/ggt431
Bowles FA (1997) Observations on attenuation and shear-wave velocity in fine-grained, marine sediments. J Acoust Soc Am 101:3385–3397. https://doi.org/10.1121/1.419374
Brocher TM (2005) Empirical relations between elastic wavespeeds and density in the Earth's crust. Bull Seismol Soc Am 95:2081–2092. https://doi.org/10.1785/0120050077
Calò M, Bodin T, Romanowicz B (2016) Layered structure in the upper mantle across North America from joint inversion of long and short period seismic data. Earth Planet Sci Lett 449:164–175. https://doi.org/10.1016/j.epsl.2016.05.054
Clayton RW, Wiggins RA (1976) Source shape estimation and devoncolution of teleseismic body waves. Geophys J R Astron Soc 47(1):151–177
Dosso SE, Dettmer J, Steininger G, Holland CW (2014) Efficient trans-dimensional Bayesian inversion for geoacoustic profile estimation. Inverse Probl 30:114018. https://doi.org/10.1088/0266-5611/30/11/114018
Evans JR, Suyehiro K, Sacks IS (1978) Mantle structure beneath the Japan Sea—A re-examination. Geophys Res Lett 5:487–490. https://doi.org/10.1029/GL005i006p00487
Frederiksen AW, Delaney C (2015) Deriving crustal properties from the P Coda without deconvolution: the southwestern Superior Province, North America. Geophys J Int 201:1491–1506. https://doi.org/10.1093/gji/ggv086
Fukao Y, Furumoto M (1975) Mechanism of large earthquakes along the eastern margin of the Japan sea. Tectonophysics 26:247–266. https://doi.org/10.1016/0040-1951(75)90093-1
Gao C, Cunningham E, Lekić V (2019) Spurious low velocity zones in joint inversions of surface waves and receiver functions. Geophys J Int 219:1032–1042. https://doi.org/10.1093/gji/ggz345
Geyer CJ, Thompson EA (1995) Annealing markov chain monte carlo with applications to ancestral inference. J Am Stat Assoc 90:909–920. https://doi.org/10.1080/01621459.1995.10476590
Green PJ (1995) Reversible jump Markov chain monte carlo computation and Bayesian model determination. Biometrika 82:711–732. https://doi.org/10.1093/biomet/82.4.711
Hamilton EL (1979) V_p / V_s and Poisson's ratios in marine sediments and rocks. J Acoust Soc Am 66:1093–1101. https://doi.org/10.1121/1.383344
Hirata N, Tokuyama H, Chung TW (1989) An anomalously thick layering of the crust of the yamato basin, southeastern sea of japan: the final stage of back-arc spreading. Tectonophysics 165:303–314. https://doi.org/10.1016/0040-1951(89)90055-3
Hopper E, Gaherty JB, Shillington DJ et al (2020) Preferential localized thinning of lithospheric mantle in the melt-poor Malawi Rift. Nat Geosci 13:584–589. https://doi.org/10.1038/s41561-020-0609-y
Van Horne A, Sato H, Ishiyama T (2017) Evolution of the Sea of Japan back-arc and some unsolved issues. Tectonophysics 710–711:6–20. https://doi.org/10.1016/j.tecto.2016.08.020
Kaneoka I, Takigami Y, Takaoka N, et al (1992) 40Ar-39Ar analysis of volcanic rocks recovered from the japan sea floor: constraints on the age of formation of the Japan Sea. In: Proceedings of the ocean drilling program, 127/128 part 2 scientific results. Ocean Drilling Program, pp 819–836
Karato S (2012) On the origin of the asthenosphere. Earth Planet Sci Lett 321–322:95–103. https://doi.org/10.1016/j.epsl.2012.01.001
Kawakatsu H, Kumar P, Takei Y et al (2009) Seismic evidence for sharp lithosphere-asthenosphere boundaries of oceanic plates. Science 324:499–502. https://doi.org/10.1126/science.1169499
Kim HJ, Lee GH, Jou HT et al (2007) Evolution of the eastern margin of Korea: Constraints on the opening of the East Sea (Japan Sea). Tectonophysics 436:37–55. https://doi.org/10.1016/j.tecto.2007.02.014
Kulinich RG, Valitov MG (2011) Thicknesses and types of the crust beneath the Sea of Japan inferred from marine and satellite gravimetric investigations. Russ J Pacific Geol 5:481–491. https://doi.org/10.1134/S1819714011060078
Kumar P, Yuan X, Kind R, Kosarev G (2005) The lithosphere-asthenosphere boundary in the Tien Shan-Karakoram region from S receiver functions: evidence for continental subduction. Geophys Res Lett 32:1–4. https://doi.org/10.1029/2004GL022291
Kumar P, Kawakatsu H, Shinohara M et al (2011) P and S receiver function analysis of seafloor borehole broadband seismic data. J Geophys Res Solid Earth 116:1–17. https://doi.org/10.1029/2011JB008506
Kurashimo E, Shinohara M, Suyehiro K et al (1996) Seismic evidence for stretched continental crust in the Japan Sea. Geophys Res Lett 23:3067–3070. https://doi.org/10.1029/96GL02765
Lekic V, French SW, Fischer KM (2011) Lithospheric thinning beneath rifted regions of Southern California. Science 334:783–787. https://doi.org/10.1126/science.1208898
Mark HF, Collins JA, Lizarralde D et al (2021) Constraints on the depth, thickness, and strength of the G discontinuity in the central pacific from s receiver functions. J Geophys Res Solid Earth 126:e2019JB019256. https://doi.org/10.1029/2019JB019256

Martin AK (2011) Double saloon door tectonics in the Japan Sea, Fossa Magna, and the Japanese Island Arc. Tectonophysics 498:45–65. https://doi.org/10.1016/j.tecto.2010.11.016
Nakahigashi K, Shinohara M, Yamada T et al (2013) Seismic structure of the extended continental crust in the Yamato Basin, Japan Sea, from ocean bottom seismometer survey. J Asian Earth Sci 67–68:199–206. https://doi.org/10.1016/j.jseaes.2013.02.028
Nakajima J, Hasegawa A (2007) Tomographic evidence for the mantle upwelling beneath southwestern Japan and its implications for arc magmatism. Earth Planet Sci Lett 254:90–105. https://doi.org/10.1016/j.epsl.2006.11.024
Nakajima J, Matsuzawa T, Hasegawa A, Zhao D (2001) Three-dimensional structure of Vp, Vs, and Vp/Vs beneath northeastern Japan: Implications for arc magmatism and fluids. J Geophys Res Solid Earth 106:21843–21857. https://doi.org/10.1029/2000JB000008
Nishizawa A, Asada A (1999) Deep crustal structure off Akita, eastern margin of the Japan Sea, deduced from ocean bottom seismographic measurements. Tectonophysics 306:199–216. https://doi.org/10.1016/S0040-1951(99)00056-6
Otofuji Y, Matsuda T, Nohda S (1985) Opening mode of the Japan Sea inferred from the palaeomagnetism of the Japan Arc. Nature 317:603–604. https://doi.org/10.1038/317603a0
Piana Agostinetti N, Malinverno A (2010) Receiver function inversion by trans-dimensional Monte Carlo sampling. Geophys J Int 181:858–872. https://doi.org/10.1111/j.1365-246X.2010.04530.x
Piana Agostinetti N, Malinverno A (2018) Assessing uncertainties in high-resolution, multifrequency receiver-function inversion: a comparison with borehole data. Geophysics 83:11–22. https://doi.org/10.1190/geo2017-0350.1
Rychert CA, Fischer KM, Rondenay S (2005) A sharp lithosphere–asthenosphere boundary imaged beneath eastern North America. Nature 436:542–545. https://doi.org/10.1038/nature03904
Rychert CA, Harmon N, Tharimena S (2018) Scattered wave imaging of the oceanic plate in cascadia. Sci Adv 4:1–8. https://doi.org/10.1126/sciadv.aao1908
Rychert CA, Harmon N, Constable S, Wang S (2020) The Nature of the lithosphere-asthenosphere boundary. J Geophys Res Solid Earth 125:1–39. https://doi.org/10.1029/2018JB016463
Rychert CA, Tharimena S, Harmon N et al (2021) A dynamic lithosphere–asthenosphere boundary near the equatorial Mid-Atlantic Ridge. Earth Planet Sci Lett 566:116949. https://doi.org/10.1016/j.epsl.2021.116949
Sambridge M (2014) A parallel tempering algorithm for probabilistic sampling and multimodal optimization. Geophys J Int 196:357–374. https://doi.org/10.1093/gji/ggt342
Sato H (1994) The relationship between Late Cenozoic tectonic events and stress field and basin development in northeast Japan. J Geophys Res Solid Earth 99:22261–22274. https://doi.org/10.1029/94JB00854
Sato T, Shinohara M, Karp BY et al (2004) P-wave velocity structure in the northern part of the central Japan Basin, Japan Sea with ocean bottom seismometers and airguns. Earth Planets Sp 56:501–510. https://doi.org/10.1186/BF03352509
Sato T, Takahashi N, Miura S et al (2006) Last stage of the Japan Sea back-arc opening deduced from the seismic velocity structure using wide-angle data. Geochem Geophys Geosyst. https://doi.org/10.1029/2005GC001135
Sato T, No T, Miura S, Kodaira S (2018) Crustal characteristic variation in the central Yamato Basin, Japan Sea back-arc basin, deduced from seismic survey results. Tectonophysics 726:1–13. https://doi.org/10.1016/j.tecto.2018.01.022
Sato T, No T, Arai R et al (2020) Transition from continental rift to back-arc basin in the southern Japan Sea deduced from seismic velocity structures. Geophys J Int 221:722–739. https://doi.org/10.1093/gji/ggaa006
Schmerr N (2012) The gutenberg discontinuity: melt at the lithosphere-asthenosphere boundary. Science 335:1480–1483. https://doi.org/10.1126/science.1215433
Seama N, Isezaki N (1990) Sea-floor magnetization in the eastern part of the Japan Basin and its tectonic implications. Tectonophysics 181:285–297. https://doi.org/10.1016/0040-1951(90)90022-Z
Sen MK, Biswas R (2017) Transdimensional seismic inversion using the reversible jump Hamiltonian Monte Carlo algorithm. Geophysics 82:R119–R134. https://doi.org/10.1190/geo2016-0010.1
Stachnik JC, Sheehan AF, Zietlow DW et al (2012) Determination of New Zealand ocean bottom seismometer orientation via Rayleigh-wave polarization. Seismol Res Lett 83:704–713. https://doi.org/10.1785/0220110128
Stein S, Stein CA (1996) Thermo-mechanical evolution of oceanic lithosphere: implications for the subduction process and deep earthquakes. Subduction Top Bottom Geophys Monogr 96:1–17. https://doi.org/10.1029/GM096p0001
Tamaki K (1985) Two modes of back-arc spreading. Geology 13:475. https://doi.org/10.1130/0091-7613(1985)13%3c475:TMOBS%3e2.0.CO;2
Tamaki K, Pisciotto K, Allan J (1990) Site 797. In: proceedings of the ODP initial reports. College Station, TX (Ocean Drilling Program), pp 323–421
Tatsumi Y, Otofuji Y, MAtsuda T, Nohda S (1989) Opening of the Sea of Japan back-arc basin by asthenopheric injection. Tectonophysics 166:317–329. https://doi.org/10.1016/0040-1951(89)90283-7
Thomson WT (1950) Transmission of elastic waves through a stratified medium. J Appl Phys 21:89–93. https://doi.org/10.1063/1.1699629
Tonegawa T, Miura S, Ishikawa A et al (2019) Characterization of crustal and uppermost-mantle seismic discontinuities in the Ontong Java Plateau. J Geophys Res Solid Earth 124:7155–7170. https://doi.org/10.1029/2018JB016970
Yoshizawa K, Miyake K, Yomogida K et al (2010) 3D upper mantle structure beneath Japan and its surrounding region from inter-station dispersion measurements of surface waves. Phys Earth Planet Inter 183:4–19. https://doi.org/10.1016/j.pepi.2010.02.012
Yu Y, Song J, Liu KH, Gao SS (2015) Determining crustal structure beneath seismic stations overlying a low-velocity sedimentary layer using receiver functions. J Geophys Res B Solid Earth 120:3208–3218. https://doi.org/10.1002/2014JB011610
Yuan X, Kind R, Li X, Wang R (2006) The S receiver functions: synthetics and data example. Geophys J Int 165:555–564. https://doi.org/10.1111/j.1365-246X.2006.02885.x
Zhang Z, Olugboji T (2021) The signature and elimination of sediment reverberations on submarine receiver functions. J Geophys Res Solid Earth 126:1–22. https://doi.org/10.1029/2020JB021567
Zheng Y, Shen W, Zhou L et al (2011) Crust and uppermost mantle beneath the North China Craton, northeastern China, and the Sea of Japan from ambient noise tomography. J Geophys Res 116:B12312. https://doi.org/10.1029/2011JB008637
Zhang R, Wu Q, Sun L et al (2014) Crustal and lithospheric structure of Northeast China from S-wave receiver functions. Earth Planet Sci Lett 401:196–205. https://doi.org/10.1016/j.epsl.2014.06.017

Publisher's Note